

## WRF and GISS SCM simulations of convective updraft properties during TWP-ICE

Jingbo Wu,<sup>1</sup> Anthony D. Del Genio,<sup>2</sup> Mao-Sung Yao,<sup>3</sup> and Audrey B. Wolf<sup>4</sup>

Received 25 July 2008; revised 8 December 2008; accepted 19 December 2008; published 27 February 2009.

[1] The Weather Research and Forecasting (WRF) model, running at cloud-resolving model resolution (1.3 km and 0.6 km), is used to simulate cumulus updraft speeds associated with three distinct convective regimes sampled during the intensive observing period of the Tropical Warm Pool–International Cloud Experiment (TWP-ICE) near Darwin, Australia. The WRF model produces strong updrafts during a monsoon break period and weaker updrafts during an active monsoon period, consistent with observational proxies of convective strength. It also captures the observed feature of midlevel convection during a suppressed monsoon period. The ability of the WRF model to differentiate the updraft speeds among three subperiods is robust to changes in its microphysics and turbulence schemes, resolution, and forcing procedure. For comparison to the parameterized diagnostic updraft speeds in the Goddard Institute for Space Studies Single Column Model (GISS SCM), we define an equivalent mean updraft speed for deep convection in the WRF simulation as the ratio of the domain average upward flux of hydrometeors to the domain average hydrometeor water content. Parameterized convective updraft speeds diagnosed from the thermodynamic structure in the SCM can reproduce the WRF difference between the active and break period updraft strength and the shallower suppressed monsoon convection, but only if a free parameter that regulates entrainment strength is allowed to vary. SCM updraft speeds are consistently too strong in the upper troposphere compared with the WRF. Hydrometeor profiles in both the WRF and the SCM are sensitive to assumptions about the ice phase microphysics.

**Citation:** Wu, J., A. D. Del Genio, M.-S. Yao, and A. B. Wolf (2009), WRF and GISS SCM simulations of convective updraft properties during TWP-ICE, *J. Geophys. Res.*, 114, D04206, doi:10.1029/2008JD010851.

### 1. Introduction

[2] Diagnosing convective updraft speeds in general circulation models (GCMs) is important for at least two reasons. First, the strength of updrafts determines the vertical transport of convective condensate and the detrainment into anvils whose microphysical and radiative properties are important to climate feedbacks [Del Genio *et al.*, 2005]. Most climate GCMs compute only the cumulus mass flux (proportional to the product of updraft speed and area). Such models cannot physically partition detrained (small hydrometeor) versus precipitated (large hydrometeor) condensate and therefore must specify an ad hoc precipitation efficiency parameter. Second, convective updraft speed regulates interactions among supercooled liquid water, graupel, and ice above the 0°C level and thereby controls

the occurrence of lightning [Petersen and Rutledge, 2001], which is a leading cause of weather-related fatalities and property damage [Curran *et al.*, 2000]. Only a few global numerical models parameterize convective updraft speeds [Sud and Walker, 1999; Bechtold *et al.*, 2001; Donner *et al.*, 2001; Jakob and Siebesma, 2003]. Most recently, a new version of the Goddard Institute for Space Studies (GISS) GCM implemented a simple estimate of convective updraft speeds. It was able to reproduce observed land-ocean differences in convective intensity and predicted significant changes in convection strength in a warmer climate [Del Genio *et al.*, 2007].

[3] Many previous studies have used convective updraft speeds to define the intensity of convection, with greater convective updraft speeds indicating a more intense storm that lofts more ice into anvils and produces more lightning [Zipser *et al.*, 2006]. It is well established that convection is stronger over land than over ocean. Zipser and Lutz [1994] have shown in composite field experiment profiles that vertical velocities near the 0°C level of 10–12 m/s are typical over land as opposed to only 4–5 m/s over ocean. Zipser *et al.* [2006] show that the Tropical Rainfall Measuring Mission (TRMM) data indicate a distinct preference for extreme intense convective events to be located over land.

<sup>1</sup>Department of Applied Physics and Applied Mathematics, Columbia University, New York, New York, USA.

<sup>2</sup>NASA Goddard Institute for Space Studies, New York, New York, USA.

<sup>3</sup>Sigma Space Partners, NASA Goddard Institute for Space Studies, New York, New York, USA.

<sup>4</sup>Center for Climate Systems Research, Columbia University, New York, New York, USA.

[4] Darwin, Australia ( $-12.4^{\circ}\text{S}$ ,  $130.9^{\circ}\text{E}$ ) is a low-latitude coastal site that experiences a wide variety of convective environments depending on whether more maritime or more continental air is being advected over the site. The convective regimes at Darwin include active monsoon periods with storms somewhat like those typical of a maritime environment; relatively suppressed monsoon periods; and monsoon break periods with occasional strong continental-type convection [May and Ballinger, 2007]. The Tropical Warm Pool–International Cloud Experiment (TWP-ICE) sampled all these environments during January–February 2006, using ground-based remote sensing instruments operated by the Australia Bureau of Meteorology and the U.S. Department of Energy Atmospheric Radiation Measurement Program (ARM). These observations were supplemented by aircraft flights and an array of atmospheric soundings that provide large-scale forcing to drive Cloud-Resolving Models (CRMs) and Single Column Models (SCMs). A description of the convective regimes during TWP-ICE, associated meteorological conditions, and the observational strategy is given by May *et al.* [2008].

[5] TWP-ICE provides a good opportunity to verify the ability of models to simulate the differences between weak versus strong and deep versus shallow convective regimes. Direct aircraft observations of convective updraft speeds were not made during TWP-ICE. Vertical motions can be retrieved from polarimetric radar data at Darwin but are not yet available. Our strategy instead is to use the Weather Research and Forecasting model (WRF) running at CRM resolution as a bridge to connect the TWP-ICE observations to SCM simulations. CRMs are increasingly being used to guide the development of climate model cloud parameterizations. Many such studies analyze CRM-simulated precipitation, heating profiles, or cloud fields [e.g., Fridlind *et al.*, 2004; Li *et al.*, 2009], but these are actually dependent on the updraft strengths of individual convective cells. In our study, we will first examine the statistics of convective updraft speeds simulated by the WRF model during TWP-ICE to see whether it can produce stronger updrafts in the break than in the active period given only differences in the thermodynamic structure. This is in itself a research question of considerable interest, since it has also been claimed that convective strength is sensitive to the aerosol load [Michalson *et al.*, 1999]. (The TWP-ICE period was characterized by generally smaller aerosol loads than were present during the earlier biomass burning season [Allen *et al.*, 2008].) We are also interested in whether the WRF can simulate the shallower congestus-type convection observed during the suppressed monsoon period, since the sensitivity of convection depth to free-troposphere humidity is known to be a weakness of SCM cumulus parameterizations [Derbyshire *et al.*, 2004]. If the WRF model can produce such differences, we can use it as a benchmark to evaluate parameterized convective updraft speeds in an SCM during the same time periods.

[6] This paper is organized as follows. Section 2 describes the surface and satellite remote sensing data sets used to evaluate the models. Sections 3 and 4 discuss the WRF model and GISS SCM physics and the setups employed for the baseline experiments. The results of simulations with both models, including various sensitivity

tests, are considered in section 5. Our conclusions and directions for further research are given in section 6.

## 2. Data

[7] The TWP-ICE SCM variational analysis forcing data [Zhang *et al.*, 2001; Xie *et al.*, 2007] (hereafter SCM forcing data) are used to drive the GISS SCM to simulate the different TWP-ICE convective regimes. The data are 3-hourly with 40 layers from 1015 to 40 mbar. In this study, three 3-day subperiods typical of each regime are simulated: 1200 UT 19 January 2006 to 1200 UT 22 January 2006 for the active period; 1200 UT 27 January 2006 to 1200 UT 30 January 2006 for the suppressed monsoon period; and 1200 UT 9 February 2006 to 1200 UT 12 February 2006 for the break period.

[8] The 6-hourly ECMWF operational analysis and forecasting system model output ([http://www.ecmwf.int/products/data/operational\\_system/index.html](http://www.ecmwf.int/products/data/operational_system/index.html)) together with temperature and moisture profiles from the SCM forcing data are used to drive the WRF model. The ECMWF product covers  $20^{\circ}\text{N}$ – $20^{\circ}\text{S}$ ,  $110^{\circ}\text{E}$ – $280^{\circ}\text{E}$  at  $0.5^{\circ}$  horizontal resolution at 15 levels from 1000 to 10 mbar.

[9] Although observations of convective updraft speeds are not available, other data provide indirect inferences about convective strength. For example, the C-Band Polarimetric Radar (C-POL) data product provides 10-min 3-D gridded reflectivity and microphysical type retrievals [May and Keenan, 2005] at a horizontal resolution of 2.5 km over a domain with a radius of 150 km and a vertical resolution of 0.5 km from 0.5 to 20 km. In addition to the greater penetration depth of high reflectivity values during strong convection, these retrievals indicate the height to which graupel extends and thus the degree to which liquid water has been lifted above the  $0^{\circ}\text{C}$  level.

[10] Lightning flash rate is another proxy for convection strength. Three dimensional locations of lightning strokes from the DLR Lightning Network (LINET) [Betz *et al.*, 2004] within a horizontal domain of  $\sim 2.5^{\circ} \times 2.5^{\circ}$  roughly centered at Darwin are considered. We first divide the domain into  $5 \text{ km} \times 5 \text{ km}$  “cells” and sum all detected strokes over each 1-min interval in each cell. Averaged over each subperiod, this gives us two observational metrics, the mean number of flashing cells and the flash rate (in flashes/min) for each flashing cell. Boccippio *et al.* [2000] suggest that distinguishing between these two metrics is important, because TRMM Lightning Imaging Sensor data indicate that the large land-ocean difference in lightning flash rate is primarily caused by the much greater spatial density of flashing cells over land and only secondarily by higher flash rates per cell.

[11] The Active Remotely Sensed Cloud Layers (ARSCL) product [Clothiaux *et al.*, 2000] is used to identify cloud top (and thus indirectly the penetration depth of convection) using the millimeter cloud radar (MMCR) [Moran *et al.*, 1998] reflectivity at 10-s resolution over 512 vertical levels. Surface precipitation data are used to distinguish heavy versus light precipitating or nonprecipitating times. Precipitation is obtained from the TWP Surface Meteorology Station (SMET) at the Central Facility, which uses conventional in situ sensors to obtain the rain rate at 1-min resolution. These data are required because ARSCL is

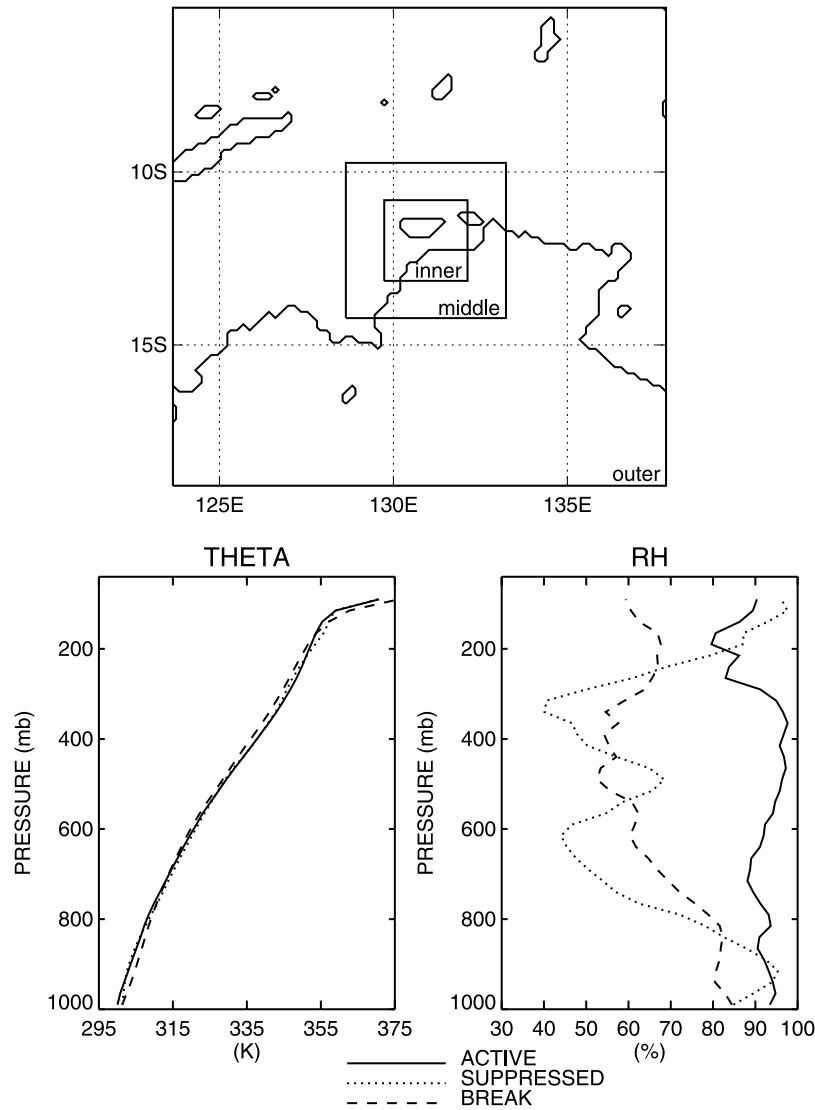


**Figure 1.** (top) Definitions of the WRF inner, middle, and outer domains used for the simulations. (bottom) (left) Mean potential temperature and (right) relative humidity profiles for each subperiod from the SCM forcing data.

sometimes attenuated in heavy rain. This problem was exacerbated during TWP-ICE by a  $\sim 15$  dBZ loss of sensitivity in the MMCR due to an earlier lightning strike (G. Mace, personal communication, 2007). Thus, we also use independent cloud top height estimates from C-POL and from MTSAT (Multifunctional Transport Satellite) visible and infrared measurements using the VISST algorithm [Minnis *et al.*, 2001, 2006]. MTSAT provides gridded data with  $0.5^\circ$  resolution from  $0^\circ$  to  $17^\circ$ S and  $125^\circ$ E– $136^\circ$ E.

### 3. WRF Model

[12] The Weather Research and Forecasting (WRF) mesoscale numerical weather prediction model with the Advanced Research WRF dynamical solver, version 2.2 [Skamarock *et al.*, 2007] is used to simulate TWP-ICE convection. The model has fully compressible nonhydrostatic equations and complete Coriolis and curvature terms. The vertical coordinate is mass-based and terrain following. The model uses Arakawa C-grid staggering. The prognostic

variables are in scalar-conserving flux form. Physics parameterization options are described in section 3.3.

#### 3.1. Standard Setup (WRF-ORIG)

[13] Initially, we set up the WRF model near the TWP-ICE Darwin area with three singly nested domains encompassing the region ( $5^\circ$ S– $19^\circ$ S,  $124^\circ$ E– $138^\circ$ E) from the surface to 50 mbar (Figure 1, top). The outer domain has  $78 \times 78$  grid boxes with 20 km horizontal resolution; the middle domain  $130 \times 130$  grid boxes with 4 km resolution; and the inner domain  $210 \times 210$  grid boxes with 1.3 km resolution. The area of the inner domain is equivalent to that of the SCM parent GCM's grid box and comparable to the scale represented by the separation distances of the six sounding locations used to derive the SCM forcing data. The ratio of the grid spacing of the 3 domains is 15:3:1. The WRF model is initialized by the ECMWF output for all three domains. Boundary conditions are updated every 6 h, using ECMWF for the outer domain and the simulations from the corresponding outer parent domains for the two

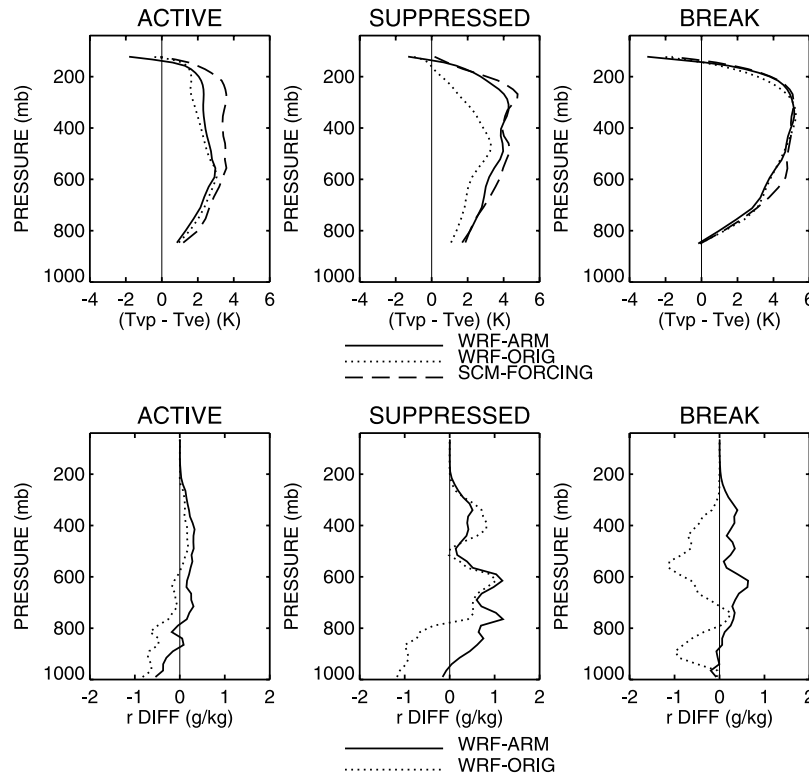


**Figure 2.** (top) Undilute parcel buoyancy profiles for each subperiod derived from the SCM forcing data and the WRF-ARM and WRF-ORIG runs with the Thompson microphysics and 50 layers. Buoyancy is calculated by finding the parcel in the lowest 3 km with the maximum equivalent potential temperature, with its properties defined as the average over a 500 m depth; lifting the parcel following a pseudoadiabatic process; and comparing the parcel virtual temperature to the environment virtual temperature. (bottom) Mean water vapor mixing ratio differences between the WRF and SCM forcing data (model minus data) for the WRF-ARM and WRF-ORIG setups.

nested domains. Excluding the initial 12-h spinup period makes little difference in our results.

[14] The SCM forcing mean thermodynamic structure during the three subperiods is shown in Figure 1 (bottom). The lapse rate is slightly more unstable during the break period than at other times, due both to a warmer boundary layer and a colder upper troposphere. The entire troposphere is almost saturated during the active period and considerably drier at other times, especially between 200 and 800 mbar. The larger undilute parcel buoyancy (following Bolton [1980]) for the break period relative to the active period in the SCM forcing data (Figure 2, top) is diagnostic of why the break period has stronger convection. Compared with the SCM forcing data, WRF inner domain simulations show large ( $\sim 1$  g/kg) dry biases in the mean water vapor mixing ratio ( $r$ ) profiles at low levels (Figure 2, bottom), which lead to underestimates in the mean convective available potential energy (CAPE) (Table 1). The CAPE error is especially large ( $\sim 900$  J/kg) for the suppressed monsoon period.

### 3.2. New Method Setup (WRF-ARM)

[15] More reliable estimates of convective updraft speeds are expected if the forcing supplied to the WRF inner domain is more closely constrained to agree with the observed SCM forcing data. We therefore tested an alternate

setup in which we retain only the inner domain. For this setup the WRF is driven with the ECMWF winds but with the ECMWF  $T$ ,  $r$  profiles replaced by the  $T$ ,  $r$  profiles from the SCM forcing data in the initial condition and at the inner domain boundaries every 6 h. The effect is somewhat similar to nudging since the reinitialized conditions at the boundary affect the inner domain over an advective time-scale. The resulting  $r$  and CAPE biases are smaller (Figure 2 and Table 1) than those from WRF-ORIG, although a nonnegligible low-level dry bias remains during the active period. It is not clear whether the remaining  $\sim 0.5$  g/kg difference between WRF and the SCM forcing is a WRF problem or a shortcoming of the forcing; the forcing humidity profiles are actually slightly wetter than several

**Table 1.** Three-Day Mean CAPE Values From the SCM Forcing Data, WRF Runs With ECMWF Forcing, and WRF Runs With ECMWF-ARM Forcing<sup>a</sup>

Mean CAPE (J/kg)	Active	Suppressed Monsoon	Break
SCM forcing	1627	1833	2094
WRF-ORIG	1056	948	1890
WRF-ARM	1138	1663	1947

<sup>a</sup>Notation: WRF runs with ECMWF forcing, WRF-ORIG; WRF runs with ECMWF-ARM forcing, WRF-ARM. CAPE is defined as the integrated buoyant energy (as defined in the Figure 2 caption) from the level of free convection up to the level of vanishing buoyancy.



**Table 2.** WRF Model Settings for Different Runs

	Horizontal Resolution (km)	Vertical Resolution (layers)	Microphysics Scheme	PBL Scheme
Thompson-30	1.33	30	Thompson	Yonsei U.
WSM6-30	1.33	30	WSM6	Yonsei U.
Lin-30	1.33	30	Purdue Lin	Yonsei U.
Thompson-30-MYJ	1.33	30	Thompson	Mellor-Yamada-Janjic
Thompson-50	1.33	50	Thompson	Yonsei U.
Thompson-fine	0.60	50	Thompson	Yonsei U.

individual sonde profiles by a similar amount. We show later that the effect of using the WRF-ORIG versus the WRF-ARM setup on the subperiod mean convective updraft speeds is fairly small, but given the improved thermodynamic structure we use the WRF-ARM setup for all other simulations described in this study.

### 3.3. Resolution and Physics Parameterizations

[16] Sensitivity to resolution and parameterized physics is tested by running the WRF with various physics packages and grid sizes (Table 2). Three microphysics schemes are compared: the WRF single moment six-class (WSM6) scheme [Hong *et al.*, 2004; Skamarock *et al.*, 2007], the Thompson scheme [Thompson *et al.*, 2004]; and the Purdue Lin scheme [Chen and Sun, 2002]. All the schemes have six classes of hydrometeors including water vapor, cloud liquid, rain, cloud ice, snow, and graupel. The Thompson scheme is intended to limit excessive snow and graupel growth in midlatitude winter environments. We also compare results using two planetary boundary layer (PBL) turbulence schemes: the Yonsei University scheme (YSU) [Hong and Pan, 1996; Skamarock *et al.*, 2007], which uses a counter-gradient flux approach for nonlocal effects, and the Mellor-Yamada-Janjic level-2.5 turbulence closure scheme (MYJ) [Mellor and Yamada, 1982; Janjic, 1990, 1996, 2002]. The YSU run uses the Monin-Obukhov surface scheme, while the MYJ run uses the Monin-Obukhov-Janjic scheme. In all runs, a thermal diffusion land surface scheme is employed [Skamarock *et al.*, 2007]. Radiation is treated using the RRTM longwave scheme, a spectral-band radiative transfer model using the correlated-k method [Mlawer *et al.*, 1997], and the Dudhia [1989] shortwave scheme. The Kain-Fritsch cumulus parameterization [Kain and Fritsch, 1993] is used in the outer domain, while moist convection is simulated explicitly in the middle and inner domains. The runs use either 30 or 50 vertical layers and 1.3 or 0.6 km horizontal resolution, with a time step of 3.3 (2.5) s at the lower (higher) horizontal resolution. Model output is sampled every 5 min.

## 4. GISS SCM

[17] The GISS SCM is based on the Goddard Institute for Space Studies (GISS) Model E GCM [Schmidt *et al.*, 2006] but with updated cloud and convection physics. The cumulus parameterization utilizes an updraft mass flux scheme with a closure that produces neutral buoyancy at cloud base. The mass flux is partitioned between two plumes entraining at different rates, as described below. The first plume is intended to represent the convective core; its entrainment rate is assumed to be lower than that of the second plume. Downdrafts are formed at any level for which an equal

mixture of updraft and environmental air is negatively buoyant; upon reaching the boundary layer, they are used to diagnose a gustiness correction to surface turbulent fluxes. A Marshall-Palmer particle size distribution is assumed for updraft condensate along with empirical size-fallspeed relations for liquid, graupel, and fluffy ice [Del Genio *et al.*, 2005]. Frozen hydrometeors are all ice at  $-40^{\circ}\text{C}$  and all graupel at  $0^{\circ}\text{C}$  with a linear transition in between.

[18] Convective updraft speeds ( $w_c$ ) in the operational model are diagnosed from the SCM gridbox thermodynamic structure using the relationship proposed by Gregory [2001],

$$\frac{1}{2} \frac{\partial w_c^2}{\partial z} = ag \left( \frac{T'_v}{T_v} - r_h \right) - \varepsilon(z) w_c^2 - bD(z) w_c^2, \quad (1)$$

where  $g$  is gravity,  $T_v$  is virtual temperature, the prime and overbar are in-cloud and environmental values,  $r_h$  is hydrometeor mixing ratio,  $D(z)$  the fractional detrainment rate due to cloud outflow,  $\varepsilon(z)$  the fractional entrainment rate, and  $a = 1/6$  and  $b = 2/3$  are dimensionless constants. Entrainment is assumed to reduce parcel buoyancy by a factor  $C$ ,

$$\varepsilon(z) w_c^2 = Cag \left( \frac{T'_v}{T_v} - r_h \right). \quad (2)$$

The two plumes are differentiated by different values of  $C$  (0.3 versus 0.6). The fraction of the particle size distribution with fallspeeds less than, comparable to, or greater than the updraft speeds determines the amount of condensate that is advected upward, detrained, or precipitated, respectively. In the GCM, this parameterization is able to distinguish strong continental from weak maritime convective updraft speeds in general agreement with field experiment composite updraft speed profiles [Del Genio *et al.*, 2007]. For our purposes a deep convective event is defined as one with continuous upward motion over a depth  $>450$  mbar.

[19] The GISS SCM has 40 layers with top at 0.1 mbar. It is driven by the SCM forcing data and reinitialized every 6 h with observed  $T, r$  profiles to avoid obscuration of the cloud response by climate drift, and to be consistent with the WRF model boundary condition updating timescale. The SCM is not spun up, because our goal is to evaluate whether it produces realistic convective updraft speeds and hydrometeor profiles given observed  $T, r$  profiles rather than to assess the fidelity of its temporal evolution. The model is sampled every half-hour time step.

[20] In addition to runs with the nominal model, we conduct several sensitivity tests varying the constant  $C$  in

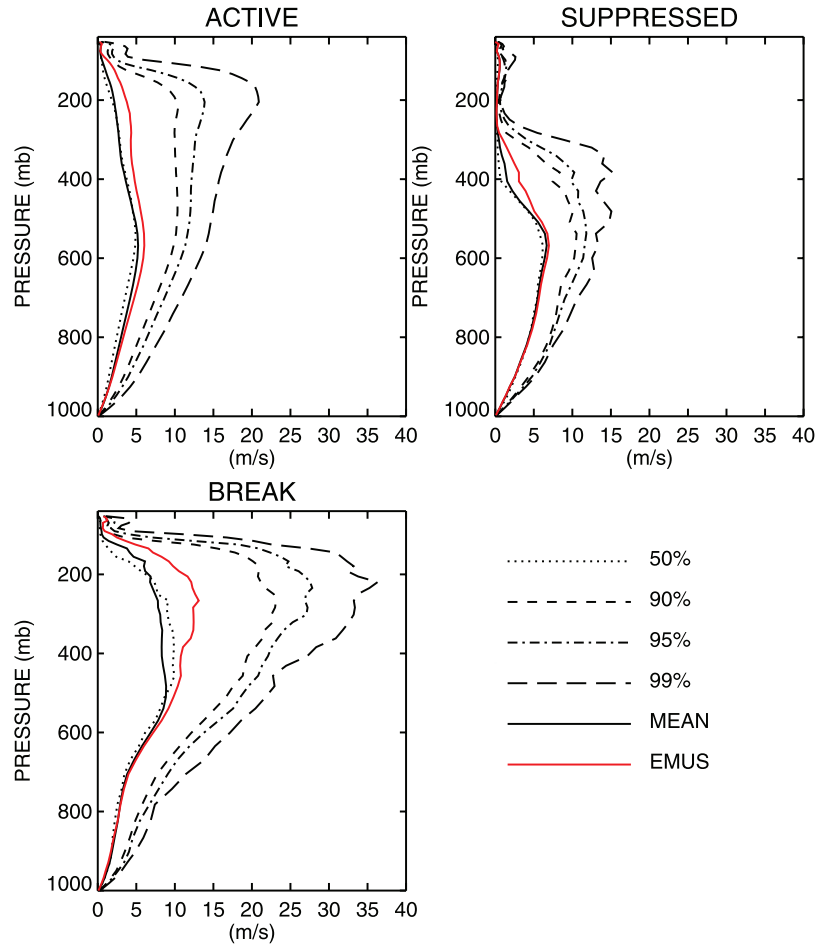


**Figure 3.** Percentiles of deep convective updraft speed from the Thompson-50 run for the active, suppressed monsoon, and break periods. The red line is the equivalent mean updraft speed profile.

the Gregory scheme that determines the magnitude of the entrainment rate in (2). We also test an alternative entrainment rate parameterization proposed by *Neggers et al.* [2002]. Neggers et al. performed large-eddy simulations (LES) of several shallow cumulus field experiment case studies and showed that at the parcel scale, the model cloud vertical structure and updraft speed profile could be approximated using an entrainment rate given by

$$\varepsilon(z) = \frac{\eta}{\tau} \frac{1}{w_c}, \quad (3)$$

where  $\tau$  is an eddy turnover timescale (taken to be 300 s) and  $\eta$  is a free parameter of  $O(1)$ . This parameterization has not to our knowledge been tested at GCM grid scales or on deep convection.

[21] We also vary assumptions made in the nominal model about the phase and size distribution of hydrometeors. Collectively we refer to these as the “new microphysics.” The new version changes the size-fallspeed relation for ice from that for dendrites to that for unrimed radiating assemblages [*Locatelli and Hobbs*, 1974], as recommended by C. Woods (personal communication, 2007). This allows ice to fall out somewhat faster. We also change the intercepts of the Marshall-Palmer distribution for

ice and graupel to those used by *Lin et al.* [1983] in their CRM microphysics, which also leads to faster fallout. We change the partitioning of ice and graupel to be a function of updraft speed so that graupel extends to higher altitude when the updraft is stronger. Finally, we change the temperature at which liquid convective condensate in rising parcels freezes from  $0^\circ\text{C}$  in the nominal model to  $-15^\circ\text{C}$ , which delays the release of latent heat owing to ice formation. The microphysics changes have a small effect on  $w_c$  through the  $r_h$  term in (1) but a substantial impact on the hydrometeor profile (and thus detrained condensate).

## 5. Simulated Updrafts in WRF and the SCM

### 5.1. Baseline Simulation

[22] For the WRF model, a deep convective column is defined as any gridbox with vertical velocity  $w \geq 1$  m/s and hydrometeor mixing ratio  $r_h \geq 10^{-4}$  kg/kg over a depth  $>450$  mbar, consistent with that used in the GISS SCM and by *Xu and Randall* [2001]. The hydrometeor threshold affects the results by  $<1$  m/s. Figure 3 shows percentiles of deep convective updraft speeds for each subperiod, using the Thompson microphysics and 50 layers. Expected differences in intensity and penetration depth among the three convective regimes are captured by WRF. Updraft speeds are weaker during the active period than during the break

period, especially in the upper troposphere. Some of the difference may be due to the underestimate of CAPE during the active period (Table 1), but the sense of the active-break difference is consistent with parcel buoyancy differences between the subperiods (Figure 2). Convection is actually strongest in the lower troposphere during the suppressed monsoon period, but most of the convection is of the midlevel congestus type, with relatively few updrafts penetrating beyond the 300 mbar level.

[23] Using this CRM information to evaluate an SCM is not straightforward. At a given timestep, an SCM only has one or a limited number of updraft speed profiles, although aggregated over time they might produce distributions of updraft speed like those in the WRF [see, e.g., *Del Genio et al.*, 2007, Figure 3]. Determining which aspect of the distribution of  $w$  is most relevant depends on the scientific application. For convective cloud feedback, our motivation for diagnosing  $w$  in a GCM is to more realistically estimate the vertical transport of hydrometeors. This depends on the competition between the updraft speeds and hydrometeor fallspeeds, which varies nonlinearly from one updraft column to another within the WRF domain.

[24] Therefore, to compare with parameterized SCM updraft speeds, we define an equivalent mean updraft speed  $w_{eq}$  for deep convection in WRF as the ratio of the domain average upward flux of hydrometeors for each half hour period (the SCM physics time step) to the domain average hydrometeor water content, and we average the result over each TWP-ICE subperiod,

$$w_{eq} = \overline{\langle wr_h \rangle} / \overline{\langle r_h \rangle}, \quad (4)$$

where  $\langle \rangle$  is the domain average over a half hour and the overbar is the 3-day subperiod time mean. In (4)  $r_h$  includes cloud liquid, rain, cloud ice, snow, and graupel. The profiles of  $w_{eq}$  are close to but slightly larger than the mean updraft speeds, most notably in the upper troposphere during the break period, because the strongest updrafts transport more large hydrometeors upward and thus detrain more condensate.

## 5.2. Comparisons With Data

[25] The most reliable aspect of a CRM simulation should be its dynamics. However, direct observations or radar retrievals of updraft speeds are not yet available for TWP-ICE, so we cannot directly validate the simulated updraft speeds in Figure 3. Our break period mean updraft speeds are several m/s stronger in the upper troposphere than core maximum vertical velocity estimates from a radar profiler over Darwin during continental conditions in an earlier year [May and Rajopadhyaya, 1999]. The 90–95th percentile WRF updraft speeds for the break period are comparable to the strongest 10% of updraft speeds reported by Zipser and Lutz [1994] for in situ measurements during a midlatitude continental field program. The WRF active period updraft speeds are several m/s stronger than those compiled by Zipser and Lutz for several tropical oceanic field experiments, but this difference seems reasonable given that the TWP-ICE active period samples coastal convection with a maritime influence rather than truly oceanic convection.

[26] We can, however, use indirect observational measures of convective depth and intensity during TWP-

ICE to get a sense of whether the simulated convection differences among the subperiods might be reasonable benchmarks for SCMs. First, we examine the WRF cloud top occurrence distribution relative to the ARM ARSCL product (Figure 4). This is not a direct measure of convective penetration depth, but it should often be close in convectively disturbed environments such as the active and break periods in which detrainment into anvils occurs near the level at which rising motion ceases. During the suppressed monsoon period, the peak near 12–13 km is instead due to cirrus advected into the Darwin area from a cyclonic disturbance to the southwest; the actual convection top is at  $\sim 9$  km (where cloud top occurrence goes to zero) or lower at this time [May et al., 2008]. The WRF cloudy area is defined as inner domain gridboxes with total cloud mixing ratio (cloud ice + cloud liquid)  $> 1 \times 10^{-6}$  kg/kg and total hydrometeor mixing ratio  $> 1 \times 10^{-4}$  kg/kg. The first criterion filters out spurious thin clouds unrelated to convection that the WRF produces above  $\sim 14$  km altitude, probably owing to errors in the SCM forcing (A. Fridlind, personal communication, 2008); the latter criterion is consistent with that applied to convective columns by Xu and Randall [2001].

[27] Surface-based cloud radar measurements may be attenuated during heavy precipitation [Naud et al., 2008]. This is especially a problem for TWP-ICE owing to the  $\sim 15$  dBZ loss of sensitivity in the MMCR. ARSCL profiles exhibit qualitative differences depending on whether the surface rain rate is  $>$  or  $\leq 0.4$  mm/h. Figure 4 shows that during times of very light or no precipitation ( $RR \leq 0.4$  mm/h), the model cloud top distribution matches ARSCL fairly well except for the lowest cloud tops. WRF cloud tops during the suppressed monsoon are somewhat lower than observed, but the simulated convection at this time extends to a level more like what is seen by ARSCL (Figure 3). During heavy precipitating events, however, the most frequently occurring ARSCL cloud top is  $\sim 6$  km lower than that in the WRF and  $\sim 3$ – $4$  km lower than that in ARSCL itself during light rain periods (only the active period is shown, but similar behavior occurs at other times).

[28] Such a large difference in the apparent attenuation for rain rates as light as 0.4 mm/h is surprising, but other indicators suggest a similar problem with ARSCL. We applied a threshold on microwave liquid water path to see whether significant within-cloud attenuation due to suspended droplets might occur even when surface rain rate was light, but this made little difference. Furthermore, independent estimates of cloud top from satellite and C-POL Radar also indicate an ARSCL bias during precipitation events. Figure 5 (top) shows the probability distribution function (PDF) of the differences between nearly coincident MTSAT infrared cloud top height and ARSCL cloud top height, separately for nonprecipitating or light-precipitating and more heavily precipitating times. Random differences between the MMCR and MTSAT are expected because they do not sample identical areas. The PDF is symmetric for nonprecipitating or light-precipitating times, with a median difference of 0.6 km. However, MTSAT cloud tops are systematically higher for heavily precipitating times, with a median difference of 2–3 km and an occasional bias as large as 6–7 km. The difference between the C-POL radar highest detected cloud top and ARSCL

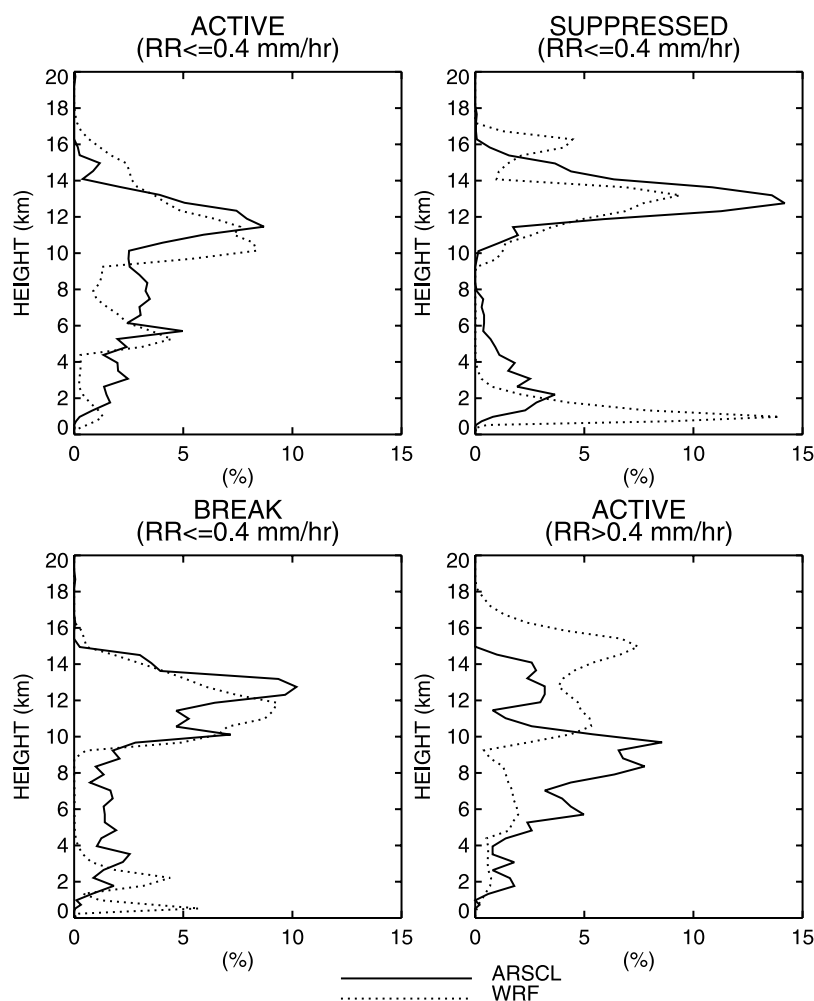


**Figure 4.** Cloud top occurrence PDFs from ARSCL and the WRF Thompson-50 runs for times with rain rate ( $RR \leq 0.4$  mm/h and for times with  $RR > 0.4$  mm/h.

(Figure 5, bottom) also supports this argument, with a median difference of 1.4 km during heavily raining periods and even larger maximum biases. During lightly precipitating or nonprecipitating periods, by contrast, C-POL slightly underestimates cloud top relative to ARSCL, consistent with the analysis of *Frederick and Schumacher* [2008].

[29] One major observed difference between active and break period convection at Darwin is the greater radar reflectivities above the  $0^{\circ}\text{C}$  level during break periods [May and Ballinger, 2007]. This is diagnostic of stronger updrafts lofting larger droplets into the upper troposphere, initiating more active mixed-phase microphysical processes. Vertical profiles of simulated hydrometeor water content (Figure 6) show that condensate is transported to higher altitude during the break simulation, as expected, but the details depend on the microphysics scheme employed. The Thompson microphysics produces enhanced condensate during the break period primarily in the middle troposphere, while the WSM-6 and Purdue Lin schemes have a larger active-break difference in the upper troposphere.

[30] The C-POL product includes 10 hydrometeor types [May and Keenan, 2005]. Graupel occurrence is of particular interest, because graupel formation requires collisions between supercooled liquid and low-density ice and is thus

diagnostic of the strength of convective updrafts. For comparison with WRF, we combine the C-POL dry graupel, wet graupel, hail, and half of the rain-hail mix into a single graupel category. The resulting graupel occurrence profiles are shown in Figure 7. The relatively high occurrence of graupel above 8 km during the break period in C-POL suggests stronger convective updraft speeds. For the WRF, the WSM-6 and Purdue Lin schemes produce too much graupel and higher graupel occurrence for the active period than for the break period. The Thompson scheme makes too little graupel, but it at least produces higher graupel occurrence for the break period relative to the active period.

[31] Finally, we examine the implications of the WRF updraft speeds for lightning production. There is considerable uncertainty about exactly how convective updraft speed is related to lightning. To compare to the LINET data, we aggregate the 1.3 km resolution WRF columns into  $5.2 \text{ km} \times 5.2 \text{ km}$  “cells” analogous to those created for the data. In each deep convective cell we average the individual updraft speed profiles into a single mean profile. We then count each cell as either flashing or nonflashing depending on whether the maximum updraft speed in the mean profile over a given temperature range exceeds a predetermined threshold. We find that a range of  $-10$  to  $-20^{\circ}\text{C}$  (roughly



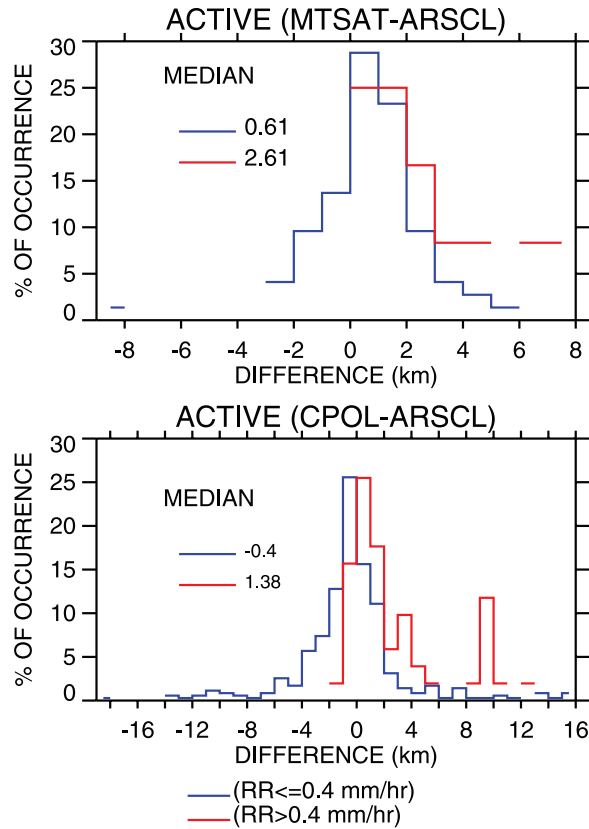


**Figure 5.** PDFs of cloud top height difference (kilometers) (top) between satellite infrared (MTSAT) and ARSCL data and (bottom) between C-POL Radar and ARSCL data for the active period. The PDFs are sorted into populations with rain rate  $\leq 0.4$  mm/h and  $>0.4$  mm/h.

consistent with the levels where most graupel is formed; see Figure 7) and a threshold updraft speed of 15 m/s (i.e., above about the 90th percentile of  $w$ , consistent with the strongest 10% of updrafts shown by Zipser and Lutz [1994]) gives the closest match to the LINET data. For cells identified as flashing in this way, we estimate the flash rate using Boccippio's [2002] "most consistent" land formula  $f = 1.52 \times 10^{-3} w^{2.67}$  (which gives much better results than his ocean relationship).

[32] For these definitions, the WRF implies slightly fewer flashing cells and higher flash rates per cell than observed, but both the model and the LINET data indicate twice as many flashing cells, and 35–40% higher flash rates per cell, during the break period than during the active period (Table 3). The total domain flash rate (the product of the number of cells and the flash rate per cell) is higher in the WRF than in the data, but both indicate  $\sim 2.8$  times as much lightning during the break period relative to the active period. This should not be considered a validation of the WRF, only a qualitative indicator that its distribution of updraft speeds is reasonable and capable of sensing the active-break differences. The results suggest that if the Boccippio [2002] relationship is corrected downward by a factor of 2, this approach might be useful for CRMs coupled to chemistry models that wish to estimate lightning production of  $\text{NO}_x$ . The lightning flash rate implied by the

equivalent mean updraft speed profile is considerably smaller (0.2 versus 1.7 fl/min for active versus break), since lightning originates from the high-end tail of the  $w$  distribution. These results suggest that WRF might be useful for developing a lightning parameterization suitable for GCMs by relating the width of the  $w$  distribution to its mean value.

### 5.3. Sensitivity Tests

[33] The results from the baseline WRF run indicate that the model is capable of simulating basic differences in the character of convection among the three TWP-ICE subperiods. However, CRMs can be sensitive to physics parameterization choices and resolution. To determine how robust WRF is as a benchmark for the SCM, we performed a series of sensitivity tests using different microphysics schemes, PBL schemes, vertical and horizontal resolutions, and forcing setups (Table 2 and Figure 8). For the active period, the equivalent mean updraft speed profiles are insensitive to changes in the microphysics scheme, PBL scheme, and resolution, with the exception of the slightly higher upper troposphere updraft speeds seen in the Purdue Lin simulation. For the break period, the strength of the updraft speeds is more sensitive to parameterized physics and resolution above the  $0^\circ\text{C}$  level, but in all cases the updrafts are still stronger than those for the active period. The differences among the break period runs are partly due to the different evolution of the thermodynamic structure over the 3-day integration period and partly a sampling issue due to the small number of convective events, as we discuss later. For the suppressed monsoon period, most runs reproduce the observed midlevel convection feature, with updraft speed differences among the runs somewhat less than for the break period; however, penetration depths are higher than ob-

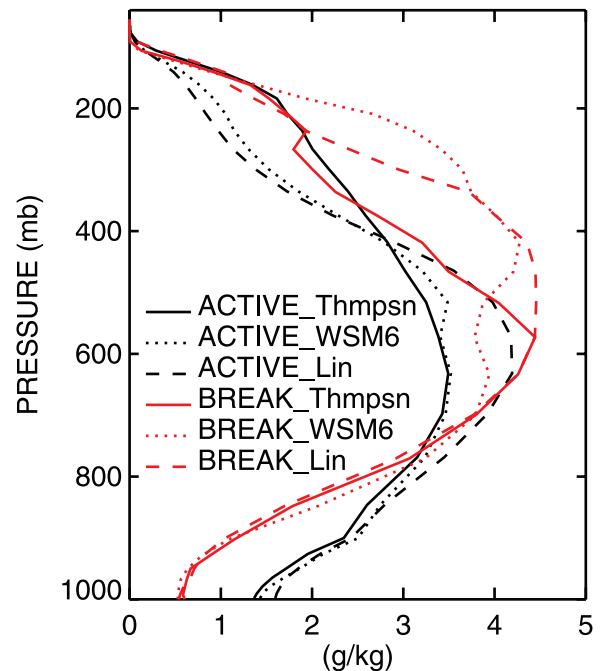


**Figure 6.** WRF hydrometeor water content profiles in deep convective cells for the active and break periods for the 30-layer Thompson, WSM-6, and Purdue Lin microphysics runs. The mean  $0^\circ\text{C}$  level is at 545 mbar.

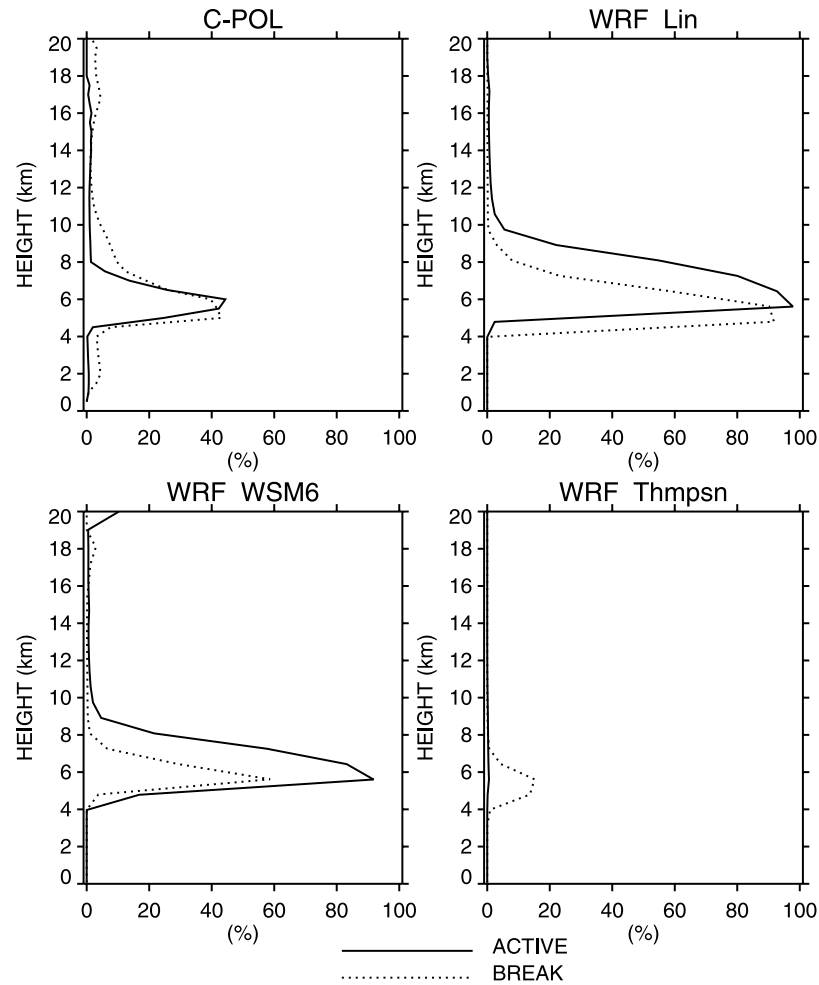


**Figure 7.** Garupel occurrence profiles from C-POL data and from the WRF Lin-30, WSM6-30, and Thompson-30 runs. The mean  $0^{\circ}\text{C}$  level is at 5.1 km.

served for the WSM-6 and Purdue Lin microphysics. For this subperiod, the results are affected by the 450 mbar thickness requirement used to identify deep convective columns, since some events are close to this depth and thus may be included or excluded from the mean profile depending on the vertical resolution and the definition employed. For example, if the thickness criterion is changed to 500 mbar, the peak in the suppressed monsoon updraft speed profile shifts upward by  $\sim 50$  mbar.

[34] Another sensitivity test compares updraft speed profiles from runs with the two different WRF model settings (WRF-ORIG and WRF-ARM) described in section 3. Figure 9 shows updraft speed profiles and temperature biases for both runs. Convective updraft speed is slightly stronger during the break period and slightly weaker during the active period when the thermodynamic structure is more tightly constrained to follow that observed (WRF-ARM), but the differences are fairly small and the sense of the active-break difference does not depend on how the inner domain is forced. For the suppressed monsoon period, on the other hand, only the WRF-ARM run is able to simulate the dominant middle-level convection. The important difference appears to be warmer temperatures and thus a slightly stronger stable layer near and above the  $0^{\circ}\text{C}$  level

(350–600 mbar) in WRF-ARM, which causes parcels to reach their level of neutral buoyancy and limits convection to the congestus stage. In WRF-ORIG, the weaker stable layer allows the convection to remain weakly buoyant near  $0^{\circ}\text{C}$  and penetrate to the upper troposphere much more often, which greatly reduces the CAPE relative to that observed (Table 1) and excessively dries the lower atmosphere (Figure 2).

[35] Finally, the algorithm to identify deep convective columns may bias the  $w_{eq}$  profiles because we only average over individual columns, which assumes that convection is upright, while in reality, updrafts are sometimes tilted with height. To investigate the extent of this bias, we consider the active period, during which  $w_{eq}$  in individual columns decreases above the 600 mbar level (Figure 3) as an example. We selected a timestep at which the  $w_{eq}$  profile

**Table 3.** Lightning Statistics From LINET Data and WRF<sup>a</sup>

	Number of Flashing Cells		Flash Rate/Cell		Domain Flash Rate	
	LINET	WRF	LINET	WRF	LINET	WRF
Active	1.9	1.5	1.1	2.7	2.1	4.0
Break	4.0	3.0	1.5	3.7	6.0	11.1

<sup>a</sup>Flash rates are in fl/min.

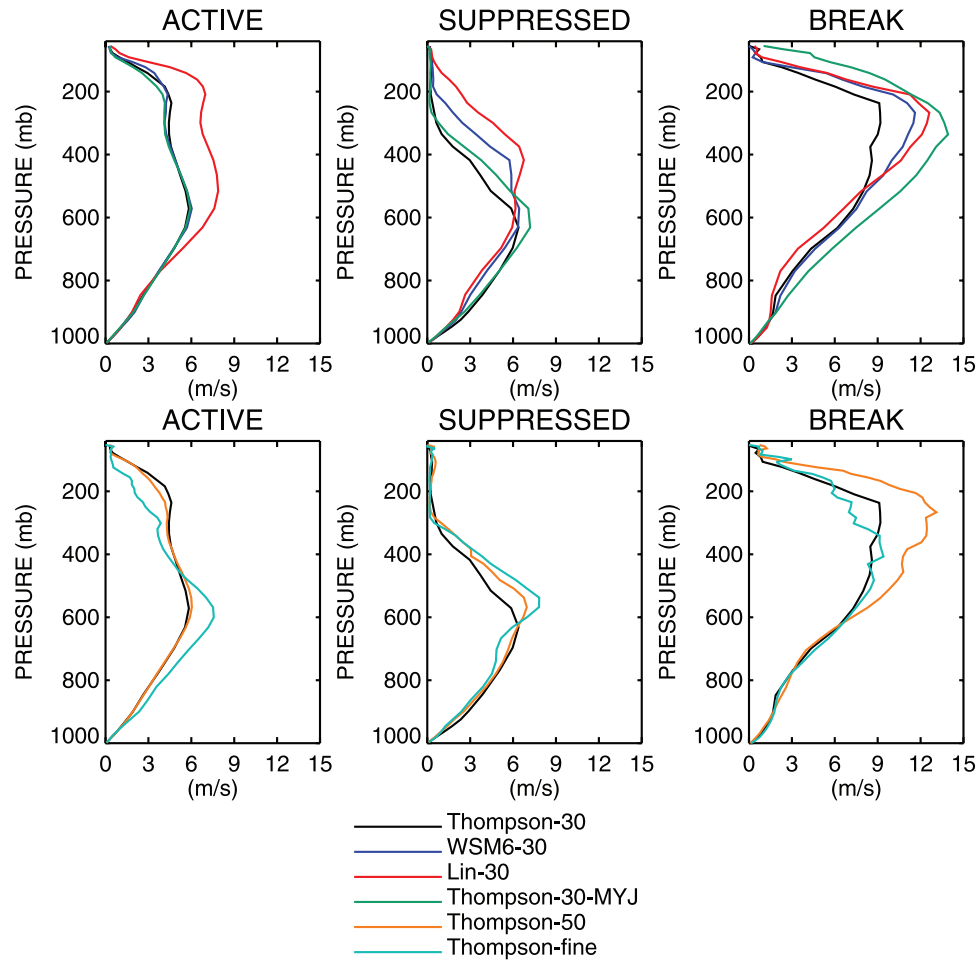


**Figure 8.** Equivalent mean updraft speed profiles for the sensitivity tests to (top) WRF physics and (bottom) resolution for the active, suppressed monsoon, and break periods.

was closest to the time mean profile seen in Figure 3 (red curve). We visually inspected each of the 19 deep updraft columns and manually recomputed the updraft speed profile along an axis defined by the maximum updraft speed at each level contiguous with the upward motion at the level below. About half of the deep convective columns have slightly tilted updrafts. The resulting adjusted profile suggests that the procedure we use to define the updraft speeds may underestimate the true speed but only by  $\sim 1$  m/s, mostly between 600 and 300 mbar. Thus, the active-break differences in Figure 3 appear to be a fairly accurate portrayal of the WRF cloud-scale dynamics.

#### 5.4. GISS SCM Simulations

[36] Figure 10 shows mean updraft speeds and entrainment rate profiles for the SCM for each subperiod using the Gregory [2001] entrainment rate formula (2) and different values of the free parameter  $C$ . For comparison, Figure 10 also shows the corresponding  $w_{eq}$  profiles derived from the WRF. For the nominal values of  $C$  (0.3, 0.6 for the first and second plumes, respectively)  $w_c$  is too strong above the freezing level during the active period and too weak during the break period, and convection penetrates too high during the suppressed monsoon. Entrainment rates during the active and suppressed monsoon periods are  $\sim 100\%/km$

near cloud base and decrease upward, similar to those inferred from a high-resolution CRM [Kuang and Bretherton, 2006]. However, the entrainment rate becomes very small ( $<10\%/km$ ) above the  $0^\circ C$  level versus  $\sim 20\%/km$  in the Kuang and Bretherton simulation, and this adversely impacts SCM updraft strength and penetration. This possible underestimate of entrainment may especially be important during the suppressed monsoon, when the midlevel environment was very dry (Figure 1) and buoyancy weak. During the break period much stronger entrainment occurs near  $\sim 800$  mbar, which prevents the SCM updraft from accelerating to the speeds simulated by the WRF above. Above the  $\sim 250$  mbar level, the updraft speeds accelerate to unrealistically high values in each subperiod.

[37] In the parent GCM, this parameterization is able to qualitatively capture observed updraft speed differences between weak oceanic and strong continental convection [Del Genio et al., 2007]. The TWP-ICE subperiod differences are more subtle and apparently beyond the scheme's capability to capture with a single parameter setting. We therefore explored the SCM's sensitivity to different values of  $C$ . Higher values for the two plumes (0.6, 0.9) reduce the excessive upper troposphere  $w_c$  during the active period to a more reasonable value and somewhat limit penetration depth during the suppressed monsoon, but at the expense

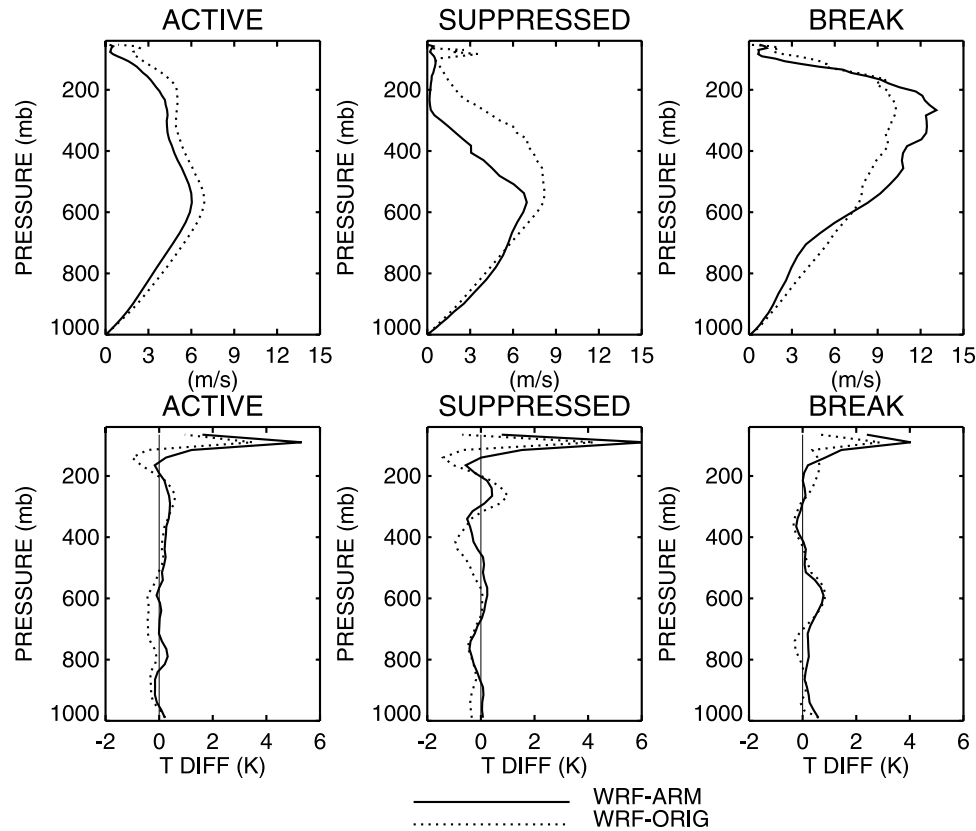


**Figure 9.** (top) Equivalent mean updraft speeds and (bottom) temperature biases relative to the SCM forcing for the three subperiods from WRF-ORIG and WRF-ARM with the Thompson scheme and 50-layer vertical resolution.

of underestimating the speed in the midtroposphere and further degrading the break period performance. Lower values of  $C$  (0.1, 0.3) produce a reasonable  $w_c$  profile for the break period up to 300 mbar but make the active and suppressed monsoon profiles worse. Replacing the old microphysical properties with the new ones has little effect on  $w_c$ . Table 4 shows the number of deep convective events simulated by the WRF (defined as the number of 30-min periods with at least one occurrence within the domain) versus that for the SCM for each subperiod. Deep convection in the WRF is widespread during the active phase and considerably less frequent during the suppressed monsoon and especially the break period, consistent with a variety of TWP-ICE observations. The SCM with the Gregory scheme best parameter settings tends to underpredict deep convection during the active period but overpredicts it at other times, especially during the suppressed monsoon.

[38] Figure 11 shows the corresponding behavior of the SCM using the Neggers *et al.* [2002] entrainment formula given by (3). We first tried the Neggers *et al.* scheme using values of its free parameter  $\eta$  that Neggers *et al.* used for shallow convection (0.9, 1.2 for the two plumes). Table 4 shows that these values produce little deep convection, and none at all during the break phase. Significantly lower values of  $\eta$  perform better, however. The active phase  $w_c$  profile is reasonably well simulated at all altitudes for  $\eta = (0.3, 0.4)$ , the suppressed monsoon with values of (0.2, 0.3), and the break with values of (0.1, 0.2). The entrainment rates for the Neggers *et al.* scheme are somewhat greater in

the middle troposphere than those for the Gregory scheme, less noisy overall, and more in line with those inferred by Kuang and Bretherton [2006], which perhaps explains its slightly better performance. Table 4 shows that the SCM with the Neggers *et al.* entrainment produces less frequent deep convection than the WRF during the active period but more frequent during the break phase.

[39] The  $T$  and  $r$  error profiles for the SCM with respect to the ARM advective forcing data set are shown in Figure 12. SCM errors are generally  $<1$  K and  $<1$  g/kg at most altitudes for all three subperiods for either entrainment scheme. The exception is the boundary layer, where the SCM produces a near-surface dry bias and compensating moist bias  $\sim 50$ –100 mbar above, and a 1–2 K near-surface warm bias. The problems are worst for the suppressed monsoon phase. The WRF simulations do not show similar error profiles (Figures 2 and 9).

[40] We believe that the SCM errors are partly related to the complex coastal environment in which TWP-ICE was conducted. The ARM SCM forcing domain is centered over land, but the sounding array includes several coastal stations and one ship [May *et al.*, 2008]. Thus the region is influenced by subgrid-scale sea breeze circulations and mesoscale convergence that sometimes drive the convection, for example, over the Tiwi Islands during the break period. This effect of surface heterogeneity cannot be captured by an SCM. It also affects the advective forcing that drives the SCM. Figure 13 (left) shows 1800 local time mean low-level soundings for the break period for each



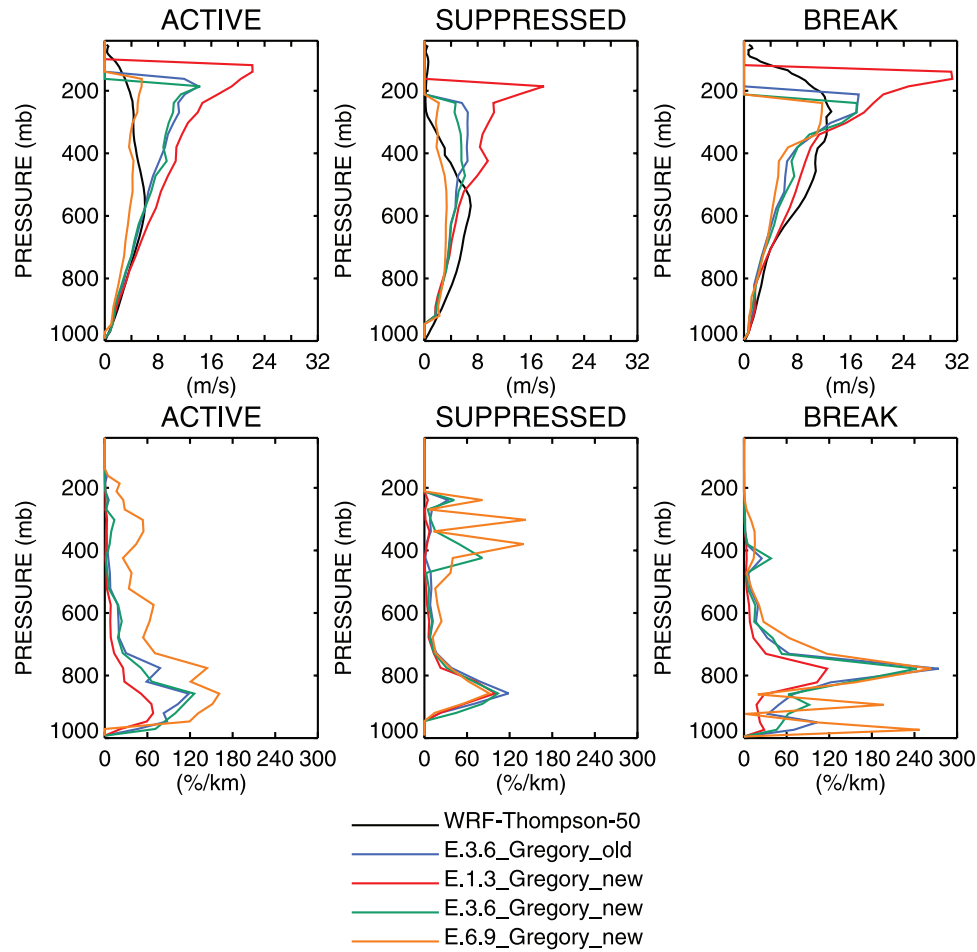


**Figure 10.** (top) Deep convective updraft speed profiles and (bottom) entrainment rate profiles for each subperiod from SCM runs using the *Gregory* [2001] entrainment rate formula with different values of the free parameter  $C$  and the old versus new microphysical properties. The top panels include the  $w_{eq}$  profile from the WRF Thompson-50 run for comparison. E.m.n in the legend indicates  $C = 0.m, 0.n$  for the two plumes.

sounding array location, and the resulting mean profile for the ARM forcing data set. The two inland stations (Point Stuart and Mt. Bundy) show an approximate mixed layer structure up to  $\sim 850$ – $900$  mbar, while the coastal and ship soundings are much more stable below the 900 mbar level. The ARM forcing data set profile is intermediate between the inland and coastal/ship profiles but its stability resembles the latter. The diurnal variation of the ARM forcing profile (not shown) is weak, in keeping with its apparent maritime/coastal character.

[41] The SCM break period diurnal cycle is shown for comparison in Figure 13 (middle). The Darwin grid point in the GISS GCM is almost totally continental. During the night and early morning its stability resembles that for the coastal/ship locations, but as the day progresses the land surface warms and the mixed layer deepens. This resembles the observed behavior at the inland stations but is not present in the ARM forcing data. This appears to be one source of the SCM temperature error and the resulting turbulent mixing is likely responsible for the dipole error pattern in the mixing ratio. We repeated the SCM runs with several experimental subdomain forcing data sets compiled

from regional subsets of the sounding array by S. Xie (personal communication, 2007), but these are only slightly different from the nominal forcing and have little effect on our results. We also tried replacing the land surface in the SCM with an ocean surface identical to that at a nearby grid point and letting the SCM calculate its own surface fluxes. In this run the break period mixing ratio error decreases to  $\sim 0.2$  g/kg or less and the surface temperature error to  $< 1$  K

**Table 4.** Number of Deep Convective Events in Each Subperiod as Simulated by the WRF 50-Layer Run With the Thompson Microphysics, and for the SCM With the New Microphysical Properties and With Various Values of the Free Parameters  $C$  and  $\eta$  in the *Gregory* [2001] and *Neggers et al.* [2002] Entrainment Formulas

Number of Events	Gregory				Neggers			
	WRF	0.1/3	0.3/6	0.6/9	0.1/2	0.2/3	0.3/4	0.9/1.2
Active	116	116	93	71	100	74	56	15
Suppressed monsoon	33	119	86	63	81	52	4	1
Break	17	39	26	13	39	18	13	0

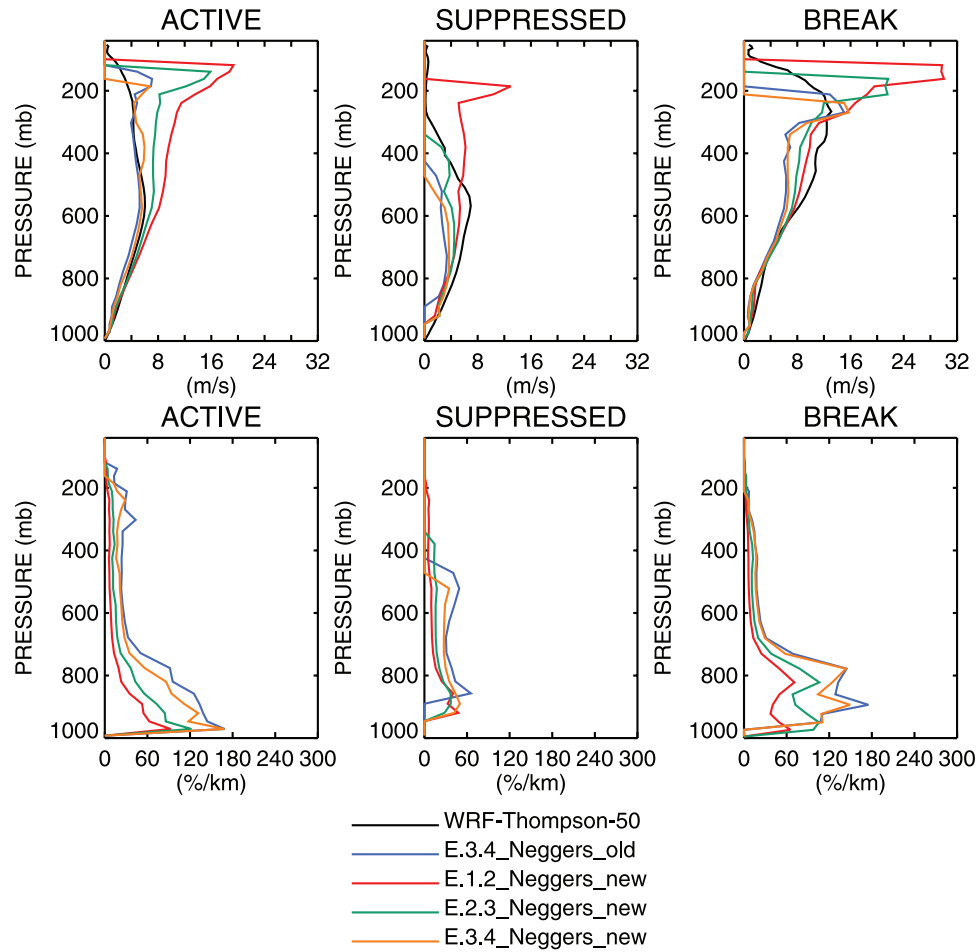


**Figure 11.** As in Figure 10 but for the *Neggers et al.* [2002] entrainment rate formula with different values of the free parameter  $\eta$ . E.m.n in the legend indicates  $\eta = 0.m, 0.n$  for the two plumes.

(Figure 12), because the SCM diurnal cycle of boundary layer temperature and depth is much weaker than in the nominal run (Figure 13). On the other hand, the same change applied to the suppressed monsoon period produces less improvement in the low-level  $T$  and  $r$  errors, and almost none at all during the active period (whose diurnal cycle is weak). Thus, we interpret the errors in Figure 12 as partly the result of the complex geography near Darwin, depending on the time period involved, but remaining errors may be due to shortcomings in the SCM physics.

[42] The ice microphysics changes we tested had little effect on the SCM updraft speed profiles because the temperature and moisture contributions to the buoyancy in the TWP-ICE environment overwhelm the negative effect of ice condensate loading. However, the microphysics changes do have a significant impact on the convective hydrometeor profile itself. This is a significant issue for GCMs, since one of the motivations for TWP-ICE was to understand how convective strength influences detrainment into the areally extensive anvil clouds that may influence cloud feedback [May et al., 2008]. Figure 14 shows the SCM hydrometeor water content profile for the best parameter settings for the Neggers et al. scheme for the active and break periods, for both the old and new microphysical properties. With the old microphysical properties there is

a minimum in water content at 400–500 mbar, and the break profile actually has less water content than the active profile above the 0°C level until convection reaches the 300 mbar level. This is at odds with the analogous WRF profiles in Figure 6 (although the WRF profile is also sensitive to the microphysics scheme used) and with the greater C-POL radar reflectivities above the freezing level during the break period. The new microphysical properties all act to produce greater particle fall speeds above the freezing level, because (1) supercooled liquid replaces ice between 0 and  $-15^{\circ}\text{C}$ , (2) more graupel and less low-density ice is assumed at higher altitude as updraft speeds increase, and (3) more graupel and low-density ice particles have large fallspeeds because of changes in the size distribution and the size-fallspeed relation. Thus, fewer hydrometeors are lofted into the upper troposphere, more are detrained in the middle troposphere, the break profile has more hydrometeor water content above the freezing level than the active, and the profiles for both periods exhibit less of a midtroposphere minimum, making them more similar to the WRF profiles.

[43] The overall in-cloud water content in the SCM exceeds that in the WRF, but for the SCM this quantity is derived from the fundamental predicted quantity, the grid-box mean water content. It is thus subject to both errors in the estimated convective cloud fraction, which we diagnose

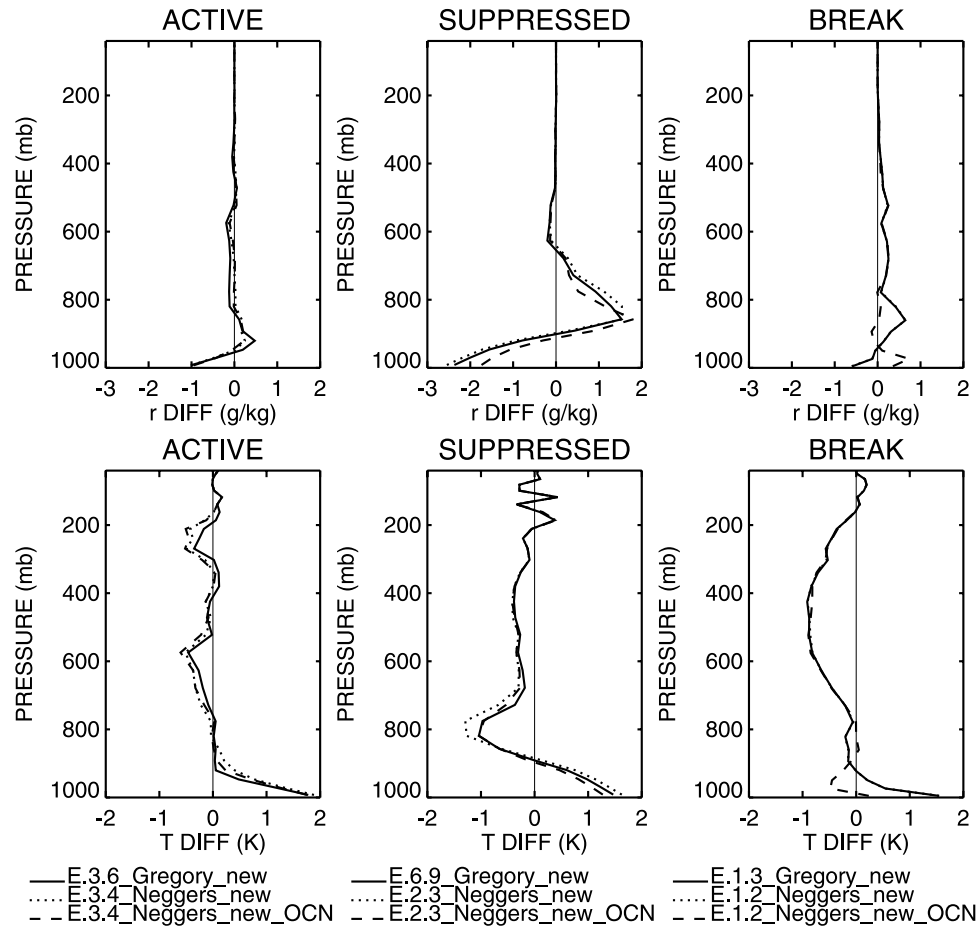


**Figure 12.** Vertical profiles of SCM water vapor mixing ratio and temperature differences with respect to the SCM forcing data set for each subperiod and for runs with the Gregory [2001] and Neggers *et al.* [2002] schemes. For the Neggers *et al.* scheme results are also shown for runs using an ocean surface.

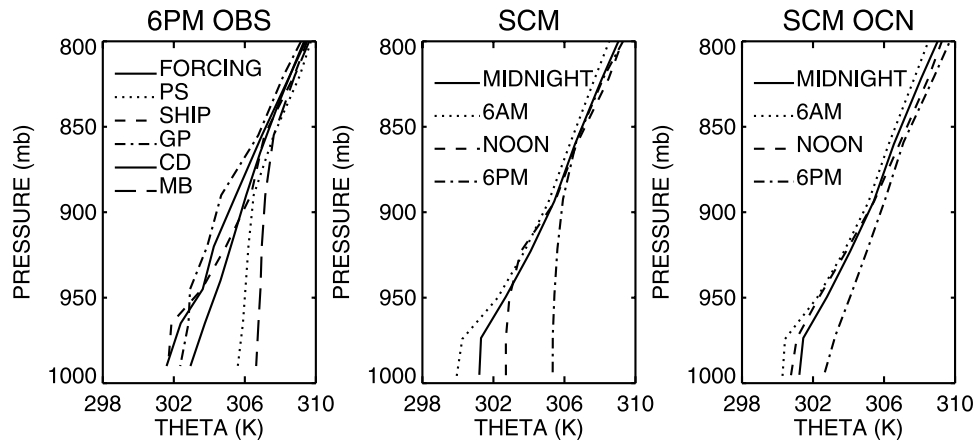


**Figure 13.** (left) Lower troposphere mean potential temperature profile at 1800 local time for the break period in the SCM forcing data set and for each of the five individual sounding locations in the TWP-ICE domain. Abbreviations are used to identify the sounding stations: PS, Point Stuart; SHIP, Ship Station; GP, Garden Point; CD, Cape Don; MB, Mount Bundy. (middle) SCM mean potential temperature profiles for the break period in the E.1.2\_Neggers\_new run at different times of day. (right) Similar to the middle panel but for a run with an ocean surface.

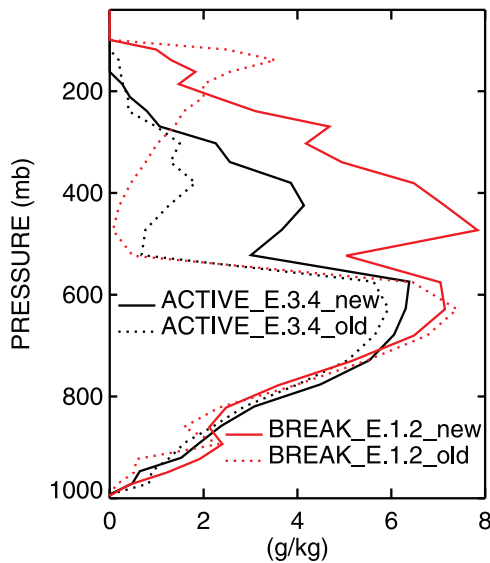


**Figure 14.** SCM hydrometeor water content profiles for the active and break periods, using the best case for each from the Neggers *et al.* [2002] scheme and the old versus new microphysics.

from the updraft speeds and mass flux but which is poorly constrained observationally, and errors in convective frequency of occurrence seen in Table 4.

## 6. Discussion and Conclusions

[44] The WRF model is able to capture both the differences in convective updraft strength between the active and break periods of the TWP-ICE experiment, with weak updrafts for the active period and strong updrafts for the break period, and also the depth of the primarily middle-level convection observed for the suppressed monsoon period. For the break period, the updraft speed is moderately sensitive to changes in resolution and parameterizations above the freezing level, but it is relatively insensitive to such changes during the active period. Overall, the ability of the WRF model to differentiate the subperiods only on the basis of differences in the thermal structure is quite robust. Simulations with different CRMs, and runs at extremely high resolution, will be required to determine whether these findings are model-specific, for example, whether the WRF's underestimate of CAPE is fundamental to this model or a symptom or errors in the forcing. However, we suggest that the WRF may provide a useful benchmark for evaluating parameterizations of updraft speed and entrainment rate for use in GCMs.

[45] The GISS SCM diagnostic updraft speed parameterization is able to capture the different convective strengths and penetration depths in the TWP-ICE subperiods using either the Gregory [2001] or Neggers *et al.* [2002] entrainment rate scheme, but only if the free parameter in each scheme is properly selected. This is a roadblock for implementing either scheme in a GCM, because cumulus parameterizations must decide on the entrainment rate when a parcel forms from boundary layer air, before its ultimate depth and strength are known. Some GCMs try to anticipate this using first guess undilute ascent estimates or large-scale

environmental indicators [Jakob and Siebesma, 2003; A. V. Maidens *et al.*, Improving mass-flux profiles in the Gregory-Rowntree convection scheme using adaptive detrainment, submitted to *Quarterly Journal of the Royal Meteorological Society*, 2009], but such approaches are in principle unsatisfactory, since the entrainment rate determines convection strength and depth.

[46] The sense of our results, taking the runs with the Neggers *et al.* [2002] mixing as an example, is that entrainment must be weakest during the break phase, slightly stronger during the less penetrative suppressed monsoon, and both must be much weaker than that simulated by Neggers *et al.* for shallow cumulus. Although we varied the free parameter  $\eta$  to accomplish this, the implication in the context of Neggers *et al.*'s approach is that their eddy turnover time  $\tau$  should be an increasing function of convection depth. This is actually consistent with the behavior of their LES model [Neggers *et al.*, 2002, Figure 4], albeit only documented over a small range of depths. Kuang and Bretherton [2006] in fact find that near cloud base, entrainment is weaker in their deep convection case than in their shallow cumulus case. One possible explanation is the deeper boundary layer that occurs in deep convective environments, which produces larger turbulent eddies that are less subject to entrainment dilution [Tokioka *et al.*, 1988]. The deepening of the SCM PBL over the course of the day seen in Figure 13 suggests that the free parameter in either entrainment scheme might usefully be scaled inversely with the boundary layer depth (as originally suggested by Tokioka *et al.*) to produce weaker entrainment in environments that produce deeper, more vigorous convection.

[47] Another possibility is that boundary layer cold pools formed by downdraft outflow organize convergence at the gust front, producing larger eddies that entrain less and allow convection to transition from shallow to deep [Tompkins, 2001; Khairoutdinov and Randall, 2006; Kuang and Bretherton, 2006]. This might explain the seemingly anomalous result from our SCM simulation of the active period, which requires stronger entrainment to produce a reasonable updraft speed profile than that needed during the break period despite comparable convection depth. Downdrafts may be less likely to form by mixing with the humid environment of the active period than with the drier air into which the break convection ascends. With less evaporation resulting from such mixing and a less unstable lapse rate during the active phase, downdrafts may be weaker and produce a smaller cold pool temperature anomaly. In addition (as suggested by a reviewer), the warmer daytime surface temperature during the break period may create a greater temperature contrast between the cold pools and their surrounding environment than during the active period, when the diurnal cycle was weaker, and this may affect the size of the eddies that result. In principle such effects can be diagnosed from the downdrafts already parameterized in the SCM.

[48] The SCM produces excessive updraft speeds above the  $\sim 250$  mbar level, regardless of entrainment rate. The Gregory [2001] diagnostic equation for  $w_c$  (1) incorporates a drag term proportional to the cumulus detrainment rate  $D(z)$  that is intended to mimic the effect of downward cloud-scale pressure gradient forces in the decelerating



region at high altitude. The GISS cumulus parameterization, however, detrains only at the cloud top level of each plume, so this term is ineffective. Several options exist for improving this aspect of the scheme. We might also include mixing detrainment at all model levels, or at least levels at which cloud-environment mixtures do not form negatively buoyant downdrafts. Another possibility is to account implicitly for the full spectrum of plume heights by replacing the cloud top forced detrainment with an “adaptive detrainment” that acts continuously with height as parcel buoyancy decreases (Maidens et al., submitted manuscript, 2009). In principle the best approach would be to parameterize the cloud-scale pressure gradient force directly as a function of grid-scale variables using the WRF simulations as a diagnostic tool, but whether this force is directly parameterizable remains to be determined.

[49] Finally, we note that the SCM with the new microphysical properties indicates that stronger convection lofts more hydrometeors into the upper troposphere and thus should detrain more ice into anvil clouds. In the WRF, one microphysics scheme produces more condensate in the middle troposphere during the break phase and two others produce more in the upper troposphere. C-POL data indicate that a much greater fraction of the radar area is covered by rain and anvil cloud during the active phase than during the break, with the ratio of the total rain (total rain + anvil cloud) area to the convective rain area being 4.9 (7.6) during the active period versus only 3.5 (5.9) for the break period [Frederick and Schumacher, 2008, Table 2]. However, this may reflect differences between subperiods in the frequency of convective events, the mesoscale condensation source, wind shear, and tropospheric humidity, as opposed to differences in the efficiency of detrainment per convective event. A better indicator of detrainment efficiency (suggested by a reviewer) might be the higher cloud tops and especially the thicker mixed anvil during the break period [Table 1 of Frederick and Schumacher, 2008]. The fundamental TWP-ICE question of the link between convection strength and upper level cloudiness thus remains an open question, requiring a complete water budget analysis for each subperiod.

[50] **Acknowledgments.** This work was supported by the DOE Atmospheric Radiation Measurement Program, NASA Precipitation Measurement Missions Program, and NASA Modeling and Analysis Program. We thank Ann Fridlind, Jay Mace, Peter May, and Shaocheng Xie for helpful discussions about the TWP-ICE data and three reviewers for constructive comments.

## References

- Allen, G., et al. (2008), Aerosol and trace-gas measurements in the Darwin area during the wet season, *J. Geophys. Res.*, **113**, D06306, doi:10.1029/2007JD008706.
- Bechtold, P., E. Bazile, F. Guichard, P. Mascart, and E. Richard (2001), A mass-flux convection scheme for regional and global models, *Q. J. R. Meteorol. Soc.*, **127**, 869–886, doi:10.1002/qj.49712757309.
- Betz, H.-D., K. Schmidt, W. P. Oettinger, and M. Wirz (2004), Lightning detection with 3D-discrimination of intracloud and cloud-to-ground discharges, *Geophys. Res. Lett.*, **31**, L11108, doi:10.1029/2004GL019821.
- Boccippio, D. J. (2002), Lightning scaling relations revisited, *J. Atmos. Sci.*, **59**, 1086–1104, doi:10.1175/1520-0469(2002)059<1086:LSRR>2.0.CO;2.
- Boccippio, D. J., S. J. Goodman, and S. Heckman (2000), The regional differences in tropical lightning distributions, *J. Appl. Meteorol.*, **39**, 2231–2248, doi:10.1175/1520-0450(2001)040<2231:RDITLD>2.0.CO;2.
- Bolton, D. (1980), The computation of equivalent potential temperature, *Mon. Weather Rev.*, **108**, 1046–1053, doi:10.1175/1520-0493(1980)108<1046:TCOEPT>2.0.CO;2.
- Chen, S.-H., and W.-Y. Sun (2002), A one-dimensional time-dependent cloud model, *J. Meteorol. Soc. Jpn.*, **80**, 99–118, doi:10.2151/jmsj.80.99.
- Clothiaux, E. E., T. P. Ackerman, G. G. Mace, K. P. Moran, R. T. Marchand, M. Miller, and B. E. Martner (2000), Objective determination of cloud heights and radar reflectivities using a combination of active remote sensors at the ARM CART sites, *J. Appl. Meteorol.*, **39**, 645–665, doi:10.1175/1520-0450(2000)039<0645:ODOCHA>2.0.CO;2.
- Curran, E. B., R. L. Holle, and R. E. Lopez (2000), Lightning casualties and damages in the United States from 1959 to 1994, *J. Clim.*, **13**, 3448–3464, doi:10.1175/1520-0442(2000)013<3448:LCADIT>2.0.CO;2.
- Del Genio, A. D., W. Kovari, M.-S. Yao, and J. Jonas (2005), Cumulus microphysics and climate sensitivity, *J. Clim.*, **18**, 2376–2387, doi:10.1175/JCLI3413.1.
- Del Genio, A. D., M.-S. Yao, and J. Jonas (2007), Will moist convection be stronger in a warmer climate?, *Geophys. Res. Lett.*, **34**, L16703, doi:10.1029/2007GL030525.
- Derbyshire, S. H., I. Beau, P. Bechtold, J. Y. Grandpeix, J. M. Piriou, J. L. Redelsperger, and P. Soares (2004), Sensitivity of moist convection to environmental humidity, *Q. J. R. Meteorol. Soc.*, **130**, 3055–3079, doi:10.1256/qj.03.130.
- Donner, L. J., C. J. Seman, and R. S. Hemler (2001), A cumulus parameterization including mass fluxes, convective vertical velocities and mesoscale effects: Thermodynamic and hydrological aspects in a general circulation model, *J. Clim.*, **14**, 3444–3463, doi:10.1175/1520-0442(2001)014<3444:ACPIMF>2.0.CO;2.
- Dudhia, J. (1989), Numerical study of convection observed during the winter monsoon experiment using a mesoscale two-dimensional model, *J. Atmos. Sci.*, **46**, 3077–3107, doi:10.1175/1520-0469(1989)046<3077:NSOCOD>2.0.CO;2.
- Frederick, K., and C. Schumacher (2008), Anvil characteristics as seen by C-POL during the Tropical Warm Pool International Cloud Experiment (TWP-ICE), *Mon. Weather Rev.*, **136**, 206–222, doi:10.1175/2007MWR2068.1.
- Fridlind, A. M., et al. (2004), Evidence for the predominance of mid-tropospheric aerosols as subtropical anvil cloud nuclei, *Science*, **304**, 718–722, doi:10.1126/science.1094947.
- Gregory, D. (2001), Estimation of entrainment rate in simple models of convective clouds, *Q. J. R. Meteorol. Soc.*, **127**, 53–72, doi:10.1002/qj.49712757104.
- Hong, S.-Y., and H.-L. Pan (1996), Nonlocal boundary layer vertical diffusion in a medium-range forecast model, *Mon. Weather Rev.*, **124**, 2322–2339, doi:10.1175/1520-0493(1996)124<2322:NBLVDI>2.0.CO;2.
- Hong, S.-Y., J. Dudhia, and S.-H. Chen (2004), A revised approach to ice microphysical processes for the bulk parameterization of clouds and precipitation, *Mon. Weather Rev.*, **132**, 103–120, doi:10.1175/1520-0493(2004)132<0103:ARATIM>2.0.CO;2.
- Jakob, C., and A. P. Siebesma (2003), A new subcloud model for mass-flux convection schemes: Influence on triggering, updraft properties, and model climate, *Mon. Weather Rev.*, **131**, 2765–2778, doi:10.1175/1520-0493(2003)131<2765:ANSMFM>2.0.CO;2.
- Janjic, Z. I. (1990), The step-mountain coordinate: Physical package, *Mon. Weather Rev.*, **118**, 1429–1443, doi:10.1175/1520-0493(1990)118<1429:TSMCPP>2.0.CO;2.
- Janjic, Z. I. (1996), The surface layer in the NCEP Eta Model, paper presented at Eleventh Conference on Numerical Weather Prediction, Am. Meteorol. Soc., Norfolk, Va.
- Janjic, Z. I. (2002), Nonsingular implementation of the Mellor–Yamada level 2.5 scheme in the NCEP Meso model, *NCEP Off. Note 437*, 61 pp., Natl. Cent. For Environ. Prediction, Camp Springs, Md.
- Kain, J. S., and J. M. Fritsch (1993), Convective parameterization for mesoscale models: The Kain-Fritsch scheme, in *The Representation of Cumulus Convection in Numerical Models*, edited by K. A. Emanuel and D. J. Raymond, pp. 165–170, Am. Meteorol. Soc., Boston, Mass.
- Khairoutdinov, M., and D. Randall (2006), High-resolution simulation of shallow-to-deep convection transition over land, *J. Atmos. Sci.*, **63**, 3421–3436, doi:10.1175/JAS3810.1.
- Kuang, Z., and C. S. Bretherton (2006), A mass-flux scheme view of a high-resolution simulation of a transition from shallow to deep cumulus convection, *J. Atmos. Sci.*, **63**, 1895–1909, doi:10.1175/JAS3723.1.
- Li, X., W.-K. Tao, A. P. Khain, J. Simpson, and D. E. Johnson (2009), Sensitivity of a cloud-resolving model to bulk and explicit bin microphysical schemes Part II: Cloud microphysics and storm dynamics interactions, *J. Atmos. Sci.*, **66**, 22–40.

- Lin, Y.-L., R. D. Farley, and H. D. Orville (1983), Bulk parameterization of the snow field in a cloud model, *J. Clim. Appl. Meteorol.*, **22**, 1065–1092, doi:10.1175/1520-0450(1983)022<1065:BPOTSF>2.0.CO;2.
- Locatelli, J. D., and P. V. Hobbs (1974), Fall speeds and masses of solid precipitation particles, *J. Geophys. Res.*, **79**, 2185–2197, doi:10.1029/JC079i015p02185.
- May, P. T., and A. Ballinger (2007), The statistical characteristics of convective cells in a monsoon regime (Darwin, Northern Australia), *Mon. Weather Rev.*, **135**, 82–92, doi:10.1175/MWR3273.1.
- May, P. T., and T. D. Keenan (2005), Evaluation of microphysical retrievals from polarimetric radar with wind profiler data, *J. Appl. Meteorol.*, **44**, 827–838, doi:10.1175/JAM2230.1.
- May, P. T., and D. K. Rajopadhyaya (1999), Vertical velocity characteristics of deep convection over Darwin, Australia, *Mon. Weather Rev.*, **127**, 1056–1071, doi:10.1175/1520-0493(1999)127<1056:VVCODC>2.0.CO;2.
- May, P. T., J. H. Mather, G. Vaughan, C. Jakob, G. M. McFarquhar, K. N. Bower, and G. G. Mace (2008), The Tropical Warm Pool International Cloud Experiment, *Bull. Am. Meteorol. Soc.*, **89**, 629–645, doi:10.1175/BAMS-89-5-629.
- Mellor, G. L., and T. Yamada (1982), Development of a turbulence closure model for geophysical fluid problems, *Rev. Geophys.*, **20**, 851–875, doi:10.1029/RG020i004p00851.
- Michalon, N., A. Nassif, T. Saouri, J. F. Royer, and C. A. Pontikis (1999), Contribution to the climatological study of lightning, *Geophys. Res. Lett.*, **26**, 3097–3100, doi:10.1029/1999GL010837.
- Minnis, P., W. L. Smith Jr., D. F. Young, L. Nguyen, A. D. Rapp, P. W. Heck, S. Sun-Mack, Q. Z. Treppe, and Y. Chen (2001), A near-real time method for deriving cloud and radiation properties from satellites for weather and climate studies, paper presented at 11th Conference on Satellite Meteorology and Oceanography, Am. Meteorol. Soc., Madison, Wis.
- Minnis, P., L. Nguyen, W. L. Smith, R. Palikonda, J. K. Ayers, D. R. Doelling, M. L. Nordeen, D. A. Spangenberg, D. N. Phan, and M. M. Khaiyer (2006), Large-scale cloud properties and radiative fluxes over Darwin during TWP-ICE, paper presented at 16th ARM Science Team Meeting, Dep. of Energy, Albuquerque, N. M.
- Mlawer, E. J., S. J. Taubman, P. D. Brown, M. J. Iacono, and S. A. Clough (1997), Radiative transfer for inhomogeneous atmosphere: RRTM, a validated correlated-k model for the longwave, *J. Geophys. Res.*, **102**, 16,663–16,682, doi:10.1029/97JD00237.
- Moran, K. P., B. E. Martner, M. J. Post, R. A. Kropfli, D. C. Welsh, and K. B. Widener (1998), An unattended cloud-profiling radar for use in climate research, *Bull. Am. Meteorol. Soc.*, **79**, 443–455, doi:10.1175/1520-0477(1998)079<0443:AUCPRF>2.0.CO;2.
- Naud, C., A. D. Del Genio, G. G. Mace, S. Benson, E. E. Clothiaux, and P. Kollias (2008), Impact of dynamics and atmospheric state on cloud vertical overlap, *J. Clim.*, **21**, 1758–1770, doi:10.1175/2007JCLI1828.1.
- Neggers, R. A. J., A. P. Siebesma, and H. J. J. Jonker (2002), A multiparcel model for shallow cumulus convection, *J. Atmos. Sci.*, **59**, 1655–1668, doi:10.1175/1520-0469(2002)059<1655:AMMFSC>2.0.CO;2.
- Petersen, W. A., and S. A. Rutledge (2001), Regional variability in tropical convection: Observations from TRMM, *J. Clim.*, **14**, 3566–3586, doi:10.1175/1520-0442(2001)014<3566:RVITCO>2.0.CO;2.
- Schmidt, G. A., et al. (2006), Present-day atmospheric simulations using GISS Model E: Comparison to in situ, satellite, and reanalysis data, *J. Clim.*, **19**, 153–192, doi:10.1175/JCLI3612.1.
- Skamarock, W. C., J. B. Klemp, J. Dudhia, D. O. Gill, D. M. Barker, W. Wang, and J. G. Powers (2007), A description of the advanced research WRF version 2, *NCAR/TN-468+STR*, 88 pp., Natl. Cent for Atmos. Res., Boulder, Colo.
- Sud, Y. C., and G. K. Walker (1999), Microphysics of clouds with the relaxed Arakawa-Schubert scheme (McRAS). Part I: Design and evaluation with GATE Phase III data, *J. Atmos. Sci.*, **56**, 3196–3220, doi:10.1175/1520-0469(1999)056<3196:MOCWTR>2.0.CO;2.
- Thompson, G., R. M. Rasmussen, and K. Manning (2004), Explicit forecasts of winter precipitation using an improved bulk microphysics scheme. Part I: Description and sensitivity analysis, *Mon. Weather Rev.*, **132**, 519–542, doi:10.1175/1520-0493(2004)132<0519:EFOWPU>2.0.CO;2.
- Tokioka, T., K. Yamazaki, A. Kitoh, and T. Ose (1988), The equatorial 30–60 day oscillation and the Arakawa-Schubert penetrative cumulus parameterization, *J. Meteorol. Soc. Jpn.*, **66**, 883–900.
- Tompkins, A. M. (2001), Organization of tropical convection in low vertical wind shears: The role of cold pools, *J. Atmos. Sci.*, **58**, 1650–1672, doi:10.1175/1520-0469(2001)058<1650:OOTCIL>2.0.CO;2.
- Xie, S., R. McCoy, S. Klein, T. Hume, C. Jakob, M. Zhang, and C. Long (2007), Objective variational analysis for the Tropical Warm Pool International Cloud Experiment, paper presented at 17th ARM Science Team Meeting, Dep. of Energy, Monterey, Calif.
- Xu, K.-M., and D. A. Randall (2001), Updraft and downdraft statistics of simulated tropical and midlatitude cumulus convection, *J. Atmos. Sci.*, **58**, 1630–1649, doi:10.1175/1520-0469(2001)058<1630:UADSOS>2.0.CO;2.
- Zhang, M. H., J. L. Lin, R. T. Cederwall, J. J. Yio, and S. C. Xie (2001), Objective analysis of ARM IOP Data: Method and sensitivity, *Mon. Weather Rev.*, **129**, 295–311, doi:10.1175/1520-0493(2001)129<0295:OAOAID>2.0.CO;2.
- Zipser, E. J., and K. R. Lutz (1994), The vertical profile of radar reflectivity of convective cells: A strong indicator of storm intensity and lightning probability?, *Mon. Weather Rev.*, **122**, 1751–1759, doi:10.1175/1520-0493(1994)122<1751:TVPORR>2.0.CO;2.
- Zipser, E. J., D. J. Cecil, C. Liu, S. W. Nesbitt, and D. P. Kory (2006), Where are the most intense thunderstorms on Earth?, *Bull. Am. Meteorol. Soc.*, **87**, 1057–1071, doi:10.1175/BAMS-87-8-1057.

A. D. Del Genio, NASA Goddard Institute for Space Studies, New York, NY 10025, USA.

A. B. Wolf, Center for Climate Systems Research, Columbia University, New York, NY 10027, USA.

J. Wu, Department of Applied Physics and Applied Mathematics, Columbia University, New York, NY 10027, USA. (jwu@giss.nasa.gov)

M.-S. Yao, Sigma Space Partners, NASA Goddard Institute for Space Studies, New York, NY 10025, USA.